CHEMISTRY OF MATERIALS

pubs.acs.org/cm

Article

Giant Low-Field Magnetocaloric Effect in the Superlattice Antiferromagnetic $ErFe_2Si_2$ Compound

D. S. Wang, X. Q. Zheng,* J. W. Xu, L. H. He, Y. W. Gao, H. Huang, H. Wu, X. Y. Cao, D. Liu, J. X. Shen, G. Y. Wang, J. Y. Zhang, Y. F. Wu, F. X. Hu, S. G. Wang,* and B. G. Shen*

Cite This: *Chem. Mater.* 2024, 36, 1707−1718

Read Online

ACCESS | Metrics & More | Article Recommendations | Supporting Information

ABSTRACT: We present herein a systematic study of a polycrystalline magnetocaloric compound $ErFe_2Si_2$. It exhibits a transition from the antiferromagnetic to the paramagnetic phase around 3.0 K according to magnetic and heat capacity measurements. Neutron powder diffraction revealed that $ErFe_2Si_2$ possesses a superlattice magnetic structure with a propagation vector of (0, 0, 0.5). The superlattice magnetic structure can be modeled by a transverse spin density wave (cosine-modulated) or a spiral type, which cannot be distinguished solely by neutron powder diffraction (NPD) pattern fitting. The stability of different types of magnetic structures was also investigated by first-principles calculations. The $ErFe_2Si_2$ compound shows a giant magnetocaloric effect with a maximal negative magnetic entropy change and an adiabatic temperature change of 11.5 J/kg K and 5.7 K, respectively, under the field change of 0−1 T. The large low-field magnetocaloric effect is related to its low critical field of metamagnetic transition and its low quasi-saturation magnetic field. The excellent performance of $ErFe_2Si_2$ makes this compound a potential magnetocaloric material for applications at liquid helium temperatures.

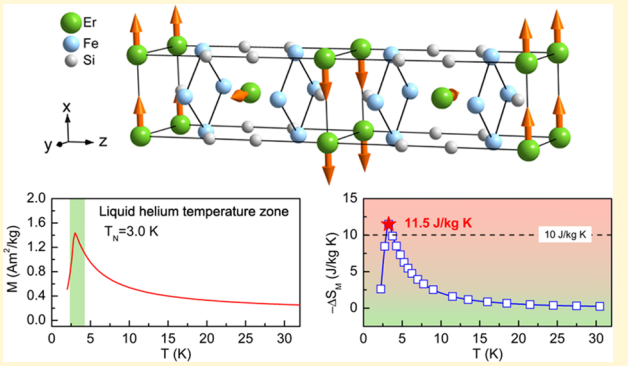

INTRODUCTION

Abundant forms of magnetic ordering exist in rare-earth-based compounds because of various magnetic couplings such as Ruderman−Kittel−Kasuya−Yosida (RKKY) indirect interaction,[1] magnetocrystalline anisotropy,[2] and magnetic quadrupole moment interaction.[3] As a result, superlattice magnetic ordering[4] as well as incommensurate magnetic ordering[5] are common, and multitudinous unconventional magnetic structures have been observed in rare-earth compounds such as transverse spin density wave (TSDW)/longitudinal spin density wave (LSDW),[6] sine-modulated,[7] spiral,[8] cycloid,[9] and conical magnetic structures.[10] The specific form of magnetic ordering plays an important role in the physical properties of rare-earth-based magnetic materials. The magnetocaloric effect (MCE) is one of the important intrinsic properties of magnetic materials, which is usually manifested as releasing or absorbing heat when the material is exposed in or removed from external magnetic fields correspondingly.[11] Since the last century, a type of cooling technology known as magnetic refrigeration or magnetic cooling based on the MCE has been developed, which is considered a promising cooling technology in the future as it is more efficient and environmentally friendly compared to the traditional cooling technology.[12] The MCE is usually evaluated by an isothermal magnetic entropy change (ΔS_M) and an adiabatic temperature change (ΔT_{ad}). A large MCE, proper working temperatures, a low driving field, and small heat/magnetic hysteresis are required and vital for the applications of magnetocaloric materials. In this work, four different types of superlattice magnetic structure including TSDW and spiral models of the rare-earth-based $ErFe_2Si_2$ compound were analyzed and a giant low-field MCE was obtained showing great competitiveness among those reported low-temperature magnetic cooling materials. The above results are shown in Figure 1 and detailed discussions will be performed in later sections.

The RFe_2Si_2 (R = rare-earth) family is a representative type of rare-earth-based compounds with rich structural and magnetic properties.[13−16] All of the RFe_2Si_2 compounds are isostructural with a $ThCr_2Si_2$-type body-centered tetragonal structure in the space group *I*4/*mmm*. In its unit cell, the rare-earth, iron, and silicon atoms occupy the 2a, 4d, and 4e sites, respectively.[13] ^{57}Fe Mössbauer spectroscopy suggests that the Fe ion contains no magnetic moment in the RFe_2Si_2 series.[14,17] Most of the RFe_2Si_2 compounds show antiferromagnetic (AFM) ordering, but a weak paramagnetic behavior is

Received: December 4, 2023
Revised: January 11, 2024
Accepted: January 11, 2024
Published: February 1, 2024

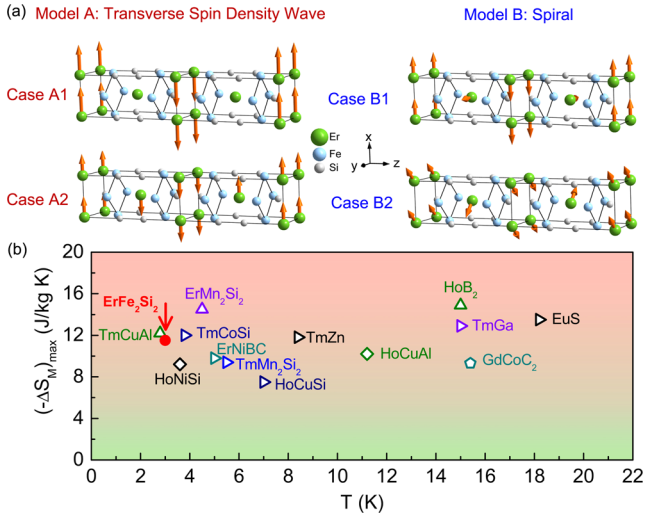

Figure 1. (a) Magnetic structures of $ErFe_2Si_2$ described using the transverse spin density wave model (model A) and the spiral model (model B). (b) Comparison of the $(-\Delta S_M)_{max}$ under a field change of 0−1 T between $ErFe_2Si_2$ and other reported low-temperature magnetocaloric materials.

observed in $LaFe_2Si_2$ and $CeFe_2Si_2$ and no long-range ordering is found in Tm and Yb compounds at 1.2 K.[13,14,16] The $ErFe_2Si_2$ compound was reported to possess a collinear AFM structure with the magnetic moment of Er atoms perpendicular to the *c*-axis and the magnetic unit cell doubling the size of the crystal unit cell according to the neutron diffraction experiment at 1.8 K.[18] However, the detailed magnetic structure and the MCE of the $ErFe_2Si_2$ compound were not further studied and reported. In this work, the detailed magnetic structure models of $ErFe_2Si_2$ including the transverse spin density wave and spiral moments are investigated and revealed, and the stability of different cases is analyzed based on the first-principles calculations. A reversible giant low-field MCE is also found in the $ErFe_2Si_2$ compound, and the peak values of the negative magnetic entropy change and the adiabatic temperature change are determined to be 11.5 J/kg K and 5.7 K, respectively, under the field change of 0−1 T.

RESULTS AND DISCUSSION

The polycrystalline $ErFe_2Si_2$ compound was synthesized by an arc-melting method. The room-temperature X-ray diffraction (XRD) pattern of the $ErFe_2Si_2$ sample is shown in Figure 2a. Rietveld refinement profile fitting indicates the formation of the high-purity single phase of $ErFe_2Si_2$ with a $ThCr_2Si_2$-type tetragonal structure (space group no. 139, *I*4/*mmm*). The lattice parameters determined from the refinement are a = 3.8930(3) Å and c = 9.9130(8) Å. Detailed refinement results show that Er, Fe, and Si atoms occupy the 2a, 4d, and 4e sites in each cell with the site symmetry of (4/*mmm*), (−4 m 2), and (4 m m), respectively, in good agreement with reported results.[18] In order to confirm the homogeneity of the sample, the element ratio in the $ErFe_2Si_2$ compound was analyzed by energy-dispersive spectroscopy (EDS) equipped on a scanning electron microscope (SEM) using both spot-scanning and area-mapping modes. The image of the microstructure for the selected area of the sample and the elemental distributions of Er, Fe, and Si are presented in Figure 2b. It can be seen that three elements are distributed homogeneously in the $ErFe_2Si_2$ compound. The EDS spectra of the two modes are shown in Figure 2c,d correspondingly. The atom ratio of Er/Fe/Si is determined to be 18.4:41.8:39.8 and 17.8:43.1:39.1 for the

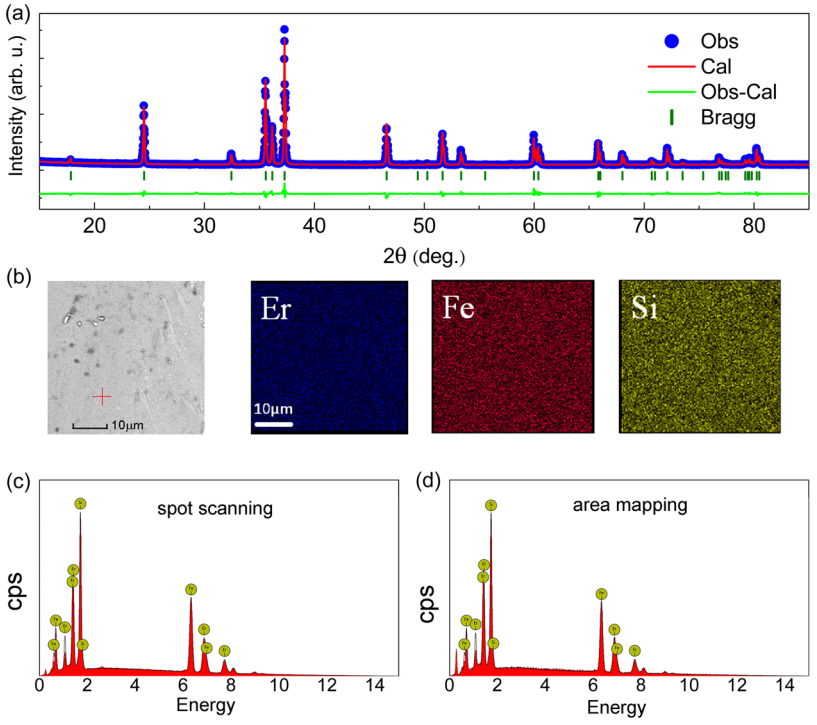

Figure 2. (a) Room-temperature X-ray diffraction (XRD) patterns and Rietveld refinement fitting of $ErFe_2Si_2$. (b) Representative image of the microstructure and the chemical element mapping for Er, Fe, and Si in the corresponding area obtained from scanning electron microscopy (SEM). (c, d) EDS spectra of $ErFe_2Si_2$ obtained from spot-scanning and area-mapping modes.

https://doi.org/10.1021/acs.chemmater.3c03079
Chem. Mater. 2024, 36, 1707−1718

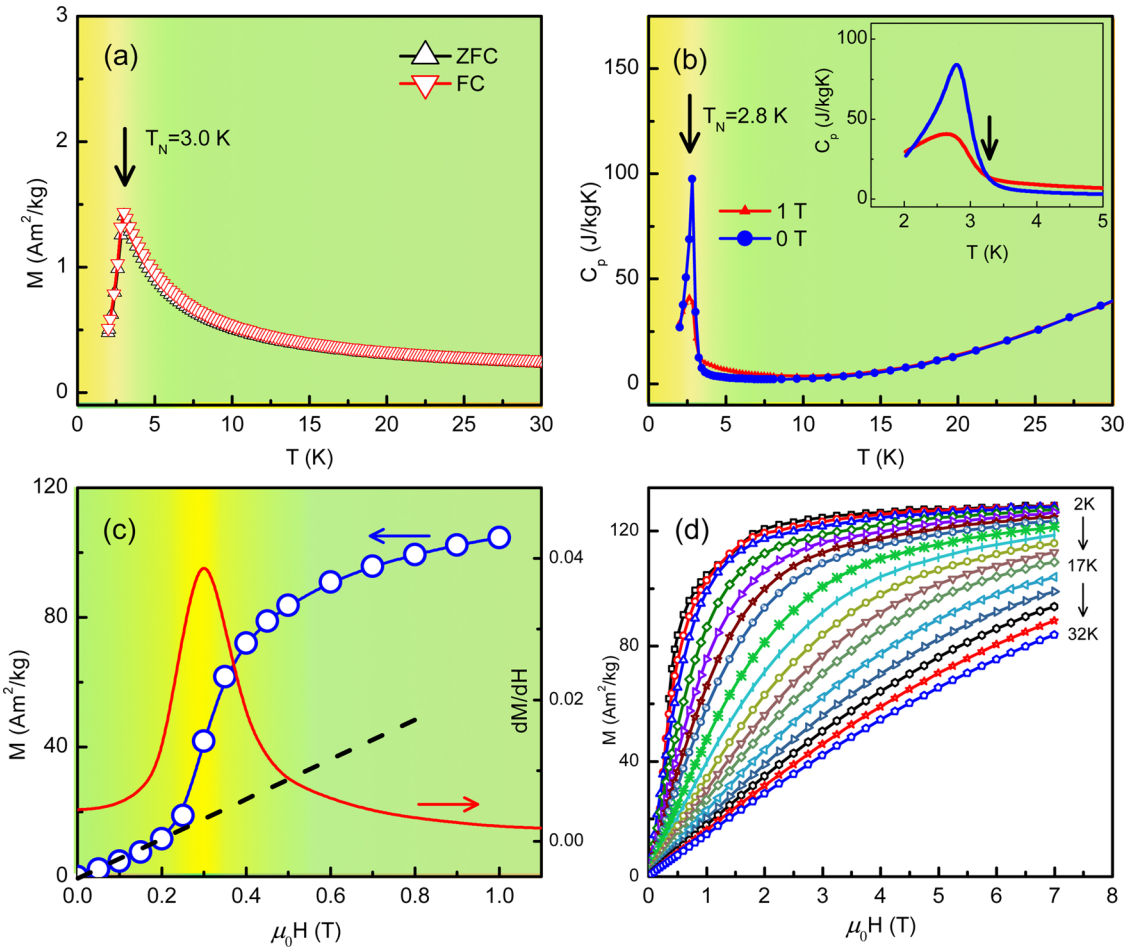

Figure 3. (a) Zero-field-cooling (ZFC) and field-cooling (FC) curves of $ErFe_2Si_2$ under the magnetic field of 0.01 T. (b) Specific heat curves of the $ErFe_2Si_2$ compound under the magnetic field of 0 and 1 T, respectively. Inset: the enlarged view of the specific heat curves around T_N. (c) Isothermal magnetization curve at 2 K and the its first-order derivative curve. (d) Isothermal magnetization curves measured at the temperatures from 2 to 32 K.

spot-scanning and area-mapping modes, respectively, close to the nominal ratio of 1:2:2.

The thermal magnetization curves of the $ErFe_2Si_2$ compound were measured under the magnetic field of 0.01 T with both zero-field-cooling (ZFC) and field-cooling (FC) modes (Figure 3a). The magnetization under both conditions increases, reaches a peak, and then decreases with increasing temperature. Such magnetization variation accords with typical antiferromagnetic behavior. The magnetic ordering temperature or Néel temperature (T_N) was determined to be 3.0 K according to the peak position in the FC curve. It should be mentioned that two characteristics in the $ErFe_2Si_2$ compound are of great importance for the magnetocaloric performance. First, its phase transition temperature is lower than the condensation point of helium gas, indicating its potential application as magnetic refrigerant materials in the liquid helium zone. Second, the ZFC and FC curves are highly consistent with each other in the whole temperature range, indicating that heat hysteresis is negligible in this material. The specific heat curves (C_p) measured at 0 and 1 T are plotted in Figure 3b. A sharp peak is clearly observed on the C_p curve under a field of 0 T, which corresponds to the antiferromagnetic (AFM) to paramagnetic (PM) transition. The peak is located at 2.8 K, close to its Néel temperature of 3.0 K. Compared to the zero-field Cp curve, a similar but less intense peak can also be observed on the C_p curve under a 1 T field, owing to the field-induced suppression of antiferromagnetic ordering. With increasing temperature, the value of C_p at 1 T overtakes that at 0 T with a cross point occurring around 3.2 K as marked in the inset of Figure 3b. This cross point has a crucial influence on the magnetocaloric effect curve, which will be discussed further in the later sections.

In order to further investigate the ground state of magnetic ordering and the magnetizing behavior of $ErFe_2Si_2$, isothermal magnetization curves (MH) of $ErFe_2Si_2$ were measured at the temperatures from 2 to 32 K. The MH curve under low fields from 0 to 1 T at 2 K is shown in Figure 3c and all of the MH curves under the full range of magnetic fields up to 7 T at different temperatures are presented in Figure 3d. From Figure 3c, it can be seen that the magnetization first increases slowly in a nearly linear relation with the magnetic field, and then it increases abruptly when the field exceeds a critical value, which is a typical characteristic of AFM compounds. The abrupt change in magnetization corresponds to the field-induced metamagnetic transition. The critical field (H_{cr}) at 2 K was determined to be 0.3 T based on the first derivative of magnetization. The critical field is so low that it is difficult to find the AFM characteristic if the MH curve is shown in the full range of the magnetic field from 0 to 7 T (Figure 3d). Another important feature of $ErFe_2Si_2$ is that it can be

https://doi.org/10.1021/acs.chemmater.3c03079
Chem. Mater. 2024, 36, 1707−1718

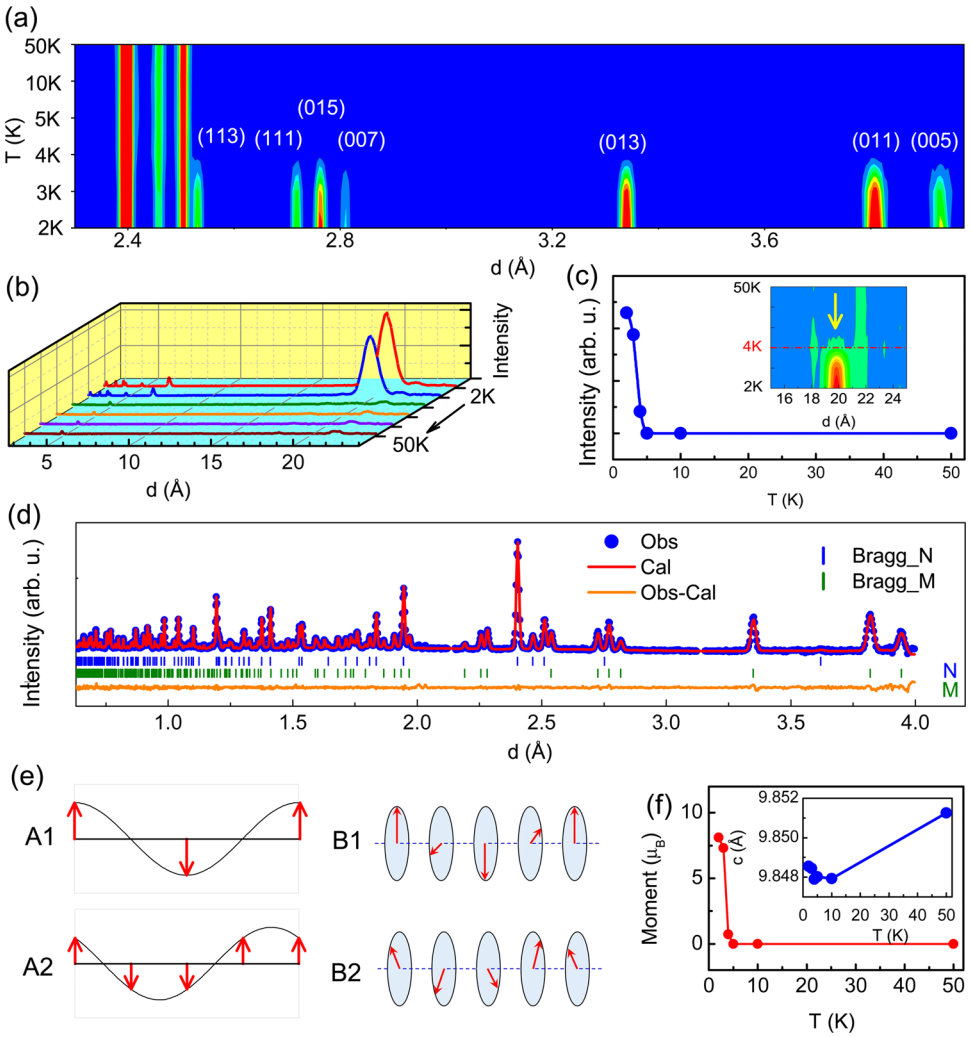

Figure 4. (a) Contour plot of the neutron powder diffraction (NPD) intensities obtained from bank A in the low d range. (b) NPD patterns at different temperatures obtained from bank B in the high d range. (c) Temperature dependence of NPD peak intensity for the representative magnetic peak. Inset: the contour plot of NPD intensity in the d-space range between 15 and 25 Å. (d) Observed NPD pattern at 2 K and the fitted curve based on Rietveld refinement of case B1. (e) Magnetic structures described by model A and model B with 4 specific cases. (f) Temperature dependence of the magnetic moment of Er atoms. Inset: the variation of the lattice parameter c with increasing temperature.

magnetized easily. Taking the MH curve at 2 K taken as an example, the magnetization at 1 T reaches 104.6 Am^2/kg, which is as high as 81.2% of that at 7 T (128.8 Am^2/kg). It indicates that magnetic ordering can be easily driven by a low magnetic field, which is significant for the performance of the low-field MCE. In addition, the MH curves at 5, 6, 7, and 8 K still exhibit obvious curvature even though they have already stepped into the PM zone. It indicates that the short-range magnetic interaction or magnetic cluster may exist in $ErFe_2Si_2$ and this characteristic is beneficial for broadening the MCE curves.[19] Furthermore, the MH curve with a decreasing field was also measured at 2 K, as shown in Figure S1. It can be seen that the MH curves with increasing and decreasing fields are almost completely coincident, indicating a good magnetic reversibility, which is in accordance with the negligible heat hysteresis observed in Figure 3a.

In order to investigate the detailed magnetic structure below T_N and the short-range magnetic interaction above T_N, neutron powder diffraction (NPD) experiments were carried out at different temperatures from 2 to 50 K. The contour plot of NPD intensity obtained from bank A is shown in Figure 4a. As it has been confirmed from the XRD result that $ErFe_2Si_2$ forms a tetragonal structure crystal structure with an $I4/mmm$ symmetry and Fe atoms occupy the 4d site, only diffraction peaks that satisfy the reflection condition $h+k+l = 2n$ will be observed under this symmetry operation. Therefore, the contributions from crystal planes (113), (111), (007), and (005) cannot be observed. In addition, although the crystal planes (015), (013), and (011) also satisfy the $h+k+l = 2n$ condition, they contain Fe atoms and the 4d Wyckoff site has an extra diffraction condition of $l = 2n$. Therefore, diffraction peaks corresponding to these crystal planes cannot be observed as well. Systematic absences of the above crystal planes can be observed at high temperatures when there is no long-range magnetic interaction anymore. The intensities of these peaks increase with decreasing temperature, indicating some likely contribution from magnetic ordering or more specific AFM ordering.

To investigate the magnetic ordering further, NPD patterns at different temperatures were also collected from bank B (Figure 4b), which can provide a higher d range. A diffraction peak with extremely high intensity can be observed at the

https://doi.org/10.1021/acs.chemmater.3c03079
Chem. Mater. 2024, 36, 1707−1718

Table 1. Comparison of the Refined Parameters Based on Model B1 (2, 3, 4 K) or the Nuclear-Only Model (5, 10, 50 K) at Different Temperatures

temperature	2 K	3 K	4 K	5 K	10 K	50 K
a (Å)	3.88784(5)	3.88785(5)	3.88812(5)	3.88804(5)	3.88814(5)	3.88789(5)
c (Å)	9.8486(2)	9.8485(2)	9.8479(3)	9.8480(3)	9.8479(3)	9.8513(3)
z_Si	0.3759(3)	0.3764(3)	0.3766(3)	0.3765(3)	0.3765(3)	0.3764(2)
M_B (μ_B)	8.12(3)	7.32(3)	0.7(3)	0	0	0
Rp (%)	2.29	2.31	2.25	2.26	2.32	2.10
Rwp (%)	2.71	2.68	2.68	2.69	2.72	2.57
χ^2	1.58	1.45	1.44	1.44	1.48	1.32

position of $d \sim 20$ Å. Since this peak can only be obviously observed at temperatures below T_N, it can rationally be ascribed to AFM ordering. Furthermore, considering that the lattice parameter c is about 9.9 Å, this AFM peak can be tentatively indexed as (0 0 1/2), suggesting the formation of a magnetic superlattice with antiferromagnetic ordering in a period of 2c. Figure 4c shows the temperature dependence of this superlattice magnetic peak intensity, and the inset shows the corresponding contour plot ranging from 15 to 25 Å. It is clear that the superlattice magnetic peak intensity decreases with increasing temperature and completely diminishes at 5 K. Considering that the Néel temperature of $ErFe_2Si_2$ is 3 K, it can be speculated that there is a short-range magnetic order at the temperatures between 3 and 5 K. A short tail observed on the contour plot at 4 K also suggests the presence of possible short-range magnetic ordering.

Rietveld refinement was carried out using the NPD patterns collected at different temperatures. Although it has been reported that $ErFe_2Si_2$ exhibits collinear AFM ordering below T_N, here we find that the magnetic structure of $ErFe_2Si_2$ cannot be determined exclusively based on NPD data. There are two models that can describe the magnetic structure of $ErFe_2Si_2$ with the same propagation vector (0, 0, 0.5). The observed NPD pattern at 2 K and the Rietveld refinement fitting curve based on one of the magnetic models are shown in Figure 4d. The first model (model A) is a cosine function-modulated magnetic structure, which is also known as the transverse spin density wave (TSDW). All of the magnetic moments are arranged in the same crystal plane and they can be described by the following formula:

$$M = M_x = M_A \times \cos(\varphi_0 + z\pi) \quad (1)$$

where M_x is the component on the x-axis of the total magnetic moment, M_A is the amplitude of the cosine-modulated magnetic structure, φ_0 is the arbitrary value of the initial phase for the cosine function, and z is the coordinate along the z-axis for Er atoms. Considering the crystal symmetry, the plane of the magnetic moments is random and equivalent only if it is parallel to the z-axis. Here, the xz plane is adopted for simplicity. In order to present the TSDW magnetic structure more specifically, two cases A1 and A2 with $\varphi_0 = 0$ and $\pi/4$, respectively, are shown in Figure 4e. For the TSDW model, the amplitude of the cosine-modulated magnetic structure (M_A) is a key parameter and TSDW is usually described by the value of $M_A/\sqrt{2}$. According to the fitting result, the value of M_A is 11.5 μ_B in both cases A1 and A2. However, the specific direction and magnitude of each Er moment may differ from each other for these two cases because of the different φ_0. For case A1, the directions of the magnetic moment are (↑ 0 ↓ 0 ↑) and the magnitudes of the magnetic moment are (11.5 0−11.5 0 11.5) μ_B for the Er atoms with z-coordinates from 0 to 2 respectively. For case A2, the directions are (↑ ↓ ↓ ↑ ↑) and the corresponding magnitudes are (8.12−8.12−8.12 8.12 8.12) μ_B. It should be noted that the magnitude of the magnetic moment is exactly $M_A/\sqrt{2}$, indicating that the A1 and A2 cases are equivalent. The second model (model B) is a spiral magnetic structure. In this situation the magnitude of the magnetic moment remains the same but its direction changes periodically in the xy plane for different Er atoms. The magnetic moments can be described by the following formula:

$$M = M_B \times e^{i(\varphi_0 + z\pi)} \quad (2)$$

where M_B is the value of the magnetic moment, φ_0 is the arbitrary value of the initial phase, and z is the coordinate along the z-axis for Er atoms, respectively. Similarly, in order to present the spiral magnetic structure more specifically, two cases B1 and B2 are shown in Figure 4e with $\varphi_0 = 0$ and $\pi/4$, respectively. For case B1, the direction of the magnetic moment is (↑ ⊙ ↓ ⊗ ↑), and the magnitude of the magnetic moment is 8.12 μ_B for all of the Er atoms with z-coordinates from 0 to 2. The fitted diffraction pattern using model B1 is presented in Figure 4d. For case B2, the magnetic moment points to the direction by rotating the corresponding magnetic moment of case B1 by $\pi/4$ in the xy plane, and the magnitude of the magnetic moment remains 8.12 μ_B.

The detailed magnetic structures corresponding to cases A1, A2, B1, and B2 are shown in Figure 1a. The observed NPD pattern at 2 K and Rietveld refinement fitted patterns based on models A1, A2, B1, and B2 are shown in Figures S2, S3, 4d, and S4, respectively. The lattice parameters, magnetic moments, estimated standard deviations (esd), and fit statistics derived from the refinement on models A1, A2, B1, and B2 are listed in the table provided in the SI. Clearly, the refinement results for all four cases including the esd are completely the same even though these models of magnetic structures are noticeably different. This indicates that these magnetic structural models cannot be distinguished from each other based solely on NPD experiments. It should be noted that case A2 has been reported as the magnetic structure of the $ErFe_2Si_2$ compound.[18] Apparently, from our studies, model A2 is not the only candidate model for the magnetic structure of $ErFe_2Si_2$. Since all of the aforementioned models show the same goodness-of-fit, model B1 was used to fit the NPD patterns at low temperatures, and the evolution of magnetic structure with temperature was investigated in detail based on model B1. While we have discussed above that $ErFe_2Si_2$ may exhibit short-range magnetic interaction at 4 K, the NPD pattern collected at 4 K can still be fitted using the long-range magnetic ordering model B1 for simplification. Both nuclear and magnetic contributions were taken into account for the refinement with the 2, 3, and 4 K patterns, and only nuclear contribution was considered for the 5, 10, and 50 K data. The

https://doi.org/10.1021/acs.chemmater.3c03079
Chem. Mater. 2024, 36, 1707−1718

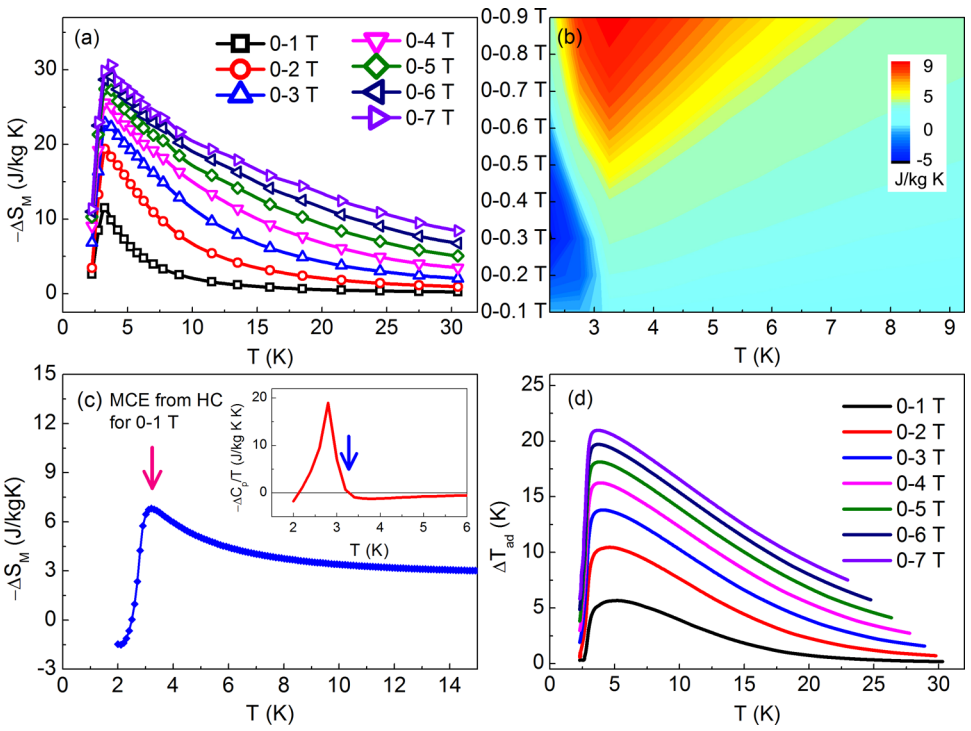

Figure 5. (a) Magnetic entropy change ($-\Delta S_M$) curves of $ErFe_2Si_2$ under different field changes. (b) Contour plot of ($-\Delta S_M$) of $ErFe_2Si_2$ under low-field changes. (c) Magnetic entropy change ($-\Delta S_M$) curve under a field change of 0−1 T calculated from the heat capacity data. Inset: the temperature dependence of $\Delta C_p/T$ for 0−1 T. (d) Adiabatic temperature change curves of $ErFe_2Si_2$ under different field changes.

observed NPD patterns at 3, 4, 5, 10, and 50 K and the corresponding Rietveld refinement fitted patterns are presented in Figures S5−S9. The refined structural parameters together with fit statistics at different temperatures are listed in Table 1. Temperature dependence of the ordered magnetic moment and the lattice parameter c is shown in Figure 4f and the inset of Figure 4f, respectively. It can be seen that the ordered magnetic moment decreases with increasing temperature. The ordered moment is calculated to be 0.7 μ_B with an error of 0.3 μ_B at 4 K, which is likely related to the aforementioned short-range magnetic interaction. Interestingly, the lattice parameter c shows a normal positive thermal expansion at high temperatures but a negative thermal expansion in the temperature range with magnetic ordering. It should be noted that no long-range Fe−Fe magnetic interaction was obtained according to the NPD experiment at different temperatures. In addition, the nearest neighboring Fe−Fe distance was also extracted from fitting results. It is found that the Fe−Fe distance is between 2.749 and 2.7495 Å at the temperatures from 2 to 50 K, which is much larger than the typical FM ordering distance between 2.4 and 2.7 Å in the La−Ce−Fe−Si−H system.[20] That is to say, the Er atom is the only origin of long-range magnetic interaction in the $ErFe_2Si_2$ compound, which is in accordance with literatures.[17,21,22] From the crystal structure of $ErFe_2Si_2$, the distance between the nearest neighboring Er atoms is positively related to the lattice parameter c and the direction of the propagation vector is also along the z-axis. Therefore, it can be predicted that a strong magnetocrystalline coupling exists in the $ErFe_2Si_2$ system. It is known that the magnetic coupling in a rare-earth-based intermetallic system is mainly dominated by RKKY interaction, in which both the type and the strength of the magnetic interaction are sensitive to the distance of magnetic atoms.[1] As a result, it can be concluded that the formation of AFM ordering will increase the distances between Er atoms. On the contrary, the destruction of AFM ordering will shrink the Er−Er distances. Furthermore, the contribution from the Er−Er distance shrinking is more significant than that from the normal thermal expansion. As a result, a negative thermal expansion is observed accompanied by magnetic ordering at low temperatures in the $ErFe_2Si_2$ compound.

The intrinsic magnetic properties of $ErFe_2Si_2$ indicate that it will show an excellent MCE at low temperatures. The primary parameter to quantitatively evaluate the MCE is known as the isothermal magnetic entropy change (ΔS_M) and it can be calculated with the isothermal magnetization data at different temperatures according to the Maxwell relation:

$$\Delta S_M(T, \Delta\mu_0 H) = \mu_0 \int_{H_1}^{H_2} \partial M/\partial T \mathrm{d}H \tag{3}$$

where H_1 and H_2 are the initial and final magnetic fields, respectively. The $-\Delta S_M$ curves under different field changes for $ErFe_2Si_2$ are shown in Figure 5a. A climax can be observed in these $-\Delta S_M$ curves at the temperature around T_N because the magnetic order just begins to be established at T_N with decreasing temperature, and the degree of magnetic ordering can be regulated most effectively among the whole temperature zone including magnetic order and magnetic disorder temperature ranges. In addition, the $-\Delta S_M$ curves are noticeably not symmetric at the two sides of T_N and there is a long tail on the high-temperature side. Such an asymmetric variation of $-\Delta S_M$ is related to the short-range interaction at the temperatures above T_N.[23] As shown in Figure 3d, there is an obvious curvature on the MH curve corresponding to the short-range magnetic ordering at temperatures above T_N, indicating that the external magnetic field can have an added effect on the extent of magnetic ordering. Consequently, a long tail can be

https://doi.org/10.1021/acs.chemmater.3c03079
Chem. Mater. 2024, 36, 1707−1718

Table 2. Magnetocaloric Parameters of $ErFe_2Si_2$ and Some Representative Refrigerant Materials Working at Similar Temperatures

		0−1 T		0−5 T		
samples	T_{ord} K	$(-\Delta S_M)_{max}$ J/kg K	ΔT_{ad} K	$(-\Delta S_M)_{max}$ J/kg K	ΔT_{ad} K	refs
$ErFe_2Si_2$	3.0	11.5	5.7	27.4	18.1	this work
HoCuSi	7.0	7.5[a]		33.1		24
$ErMn_2Si_2$	4.5	14.5	2.5	25.2	12.9	25
$TmMn_2Si_2$	5.5	9.4	2.7	22.7	10.1	26
TmZn	8.4	11.8		26.9	8.6	27
TmCuAl	2.8	12.2		24.3	9.4	28
TmCoSi	3.8	12.0	6.2	22.1	17.3	29
HoB_2	15.0	14.9[a]	3.5[a]	40.1	12.0	30
TmGa	15.0	12.9	3.2	34.2	9.1	31
EuS	18.2	13.5[a]	7.5	37.0	10.4	32
HoCuAl	11.2	10.2[a]		30.6		33
$GdCoC_2$	15	9.3		28.4		34
HoNiSi	3.8	9.2		26.0	8.5	35
ErNiBC	5.0	9.8	2.7	24.8	8.6	36

[a]These results are estimated from the relevant references.

observed on the $-\Delta S_M$ curves of $ErFe_2Si_2$ with extension of the short-range magnetic ordering into the temperature region above T_N.

The maximum value of the magnetic entropy change ($(-\Delta S_M)_{max}$) is usually considered the key MCE parameter for magnetocaloric materials. The $(-\Delta S_M)_{max}$ values of $ErFe_2Si_2$ are calculated to be 11.5, 19.4, 22.9, 25.6, 27.4, 29.1, and 30.7 J/kg K under the field changes of 0−1, 0−2, 0−3, 0−4, 0−5, 0−6, and 0−7 T, respectively. To compare the $(-\Delta S_M)_{max}$ of $ErFe_2Si_2$ with those of other low-temperature magnetocaloric materials, the MCE parameters of the representative refrigerant materials with low working temperatures are listed in Table 2. Most of the parameters are directly cited from references and some parameters marked with stars are estimated from the figures in the relevant references.[24−36] It can be seen that the $(-\Delta S_M)_{max}$ of $ErFe_2Si_2$ under a field change of 0−5 T is comparable or even larger than those of the listed materials. It should be noted that the magnetic entropy change under low-field variation, for example 0−1 T, has a greater reference significance for practical applications. On one hand, the maximum magnetic field used in magnetic refrigerators is usually no more than 1.5 T.[37−39] On the other hand, though it is true that the applied magnetic field at low temperatures may be quite large based on superconductors, the magnetic refrigerant materials with a large low-field MCE are still important because they can lower the cost. Although the $(-\Delta S_M)_{max}$ of $ErFe_2Si_2$ is smaller than those of HoCuSi, HoCuAl, and $GdCoC_2$ under a field change of 0−5 T, $ErFe_2Si_2$ shows a larger $(-\Delta S_M)_{max}$ than these compounds under a field change of 0−1 T. It means that $ErFe_2Si_2$ exhibits a giant low-field MCE. To further analyze the low-field MCE of the $ErFe_2Si_2$ compound, the value of the $(-\Delta S_M)_{max}$ under a field change of 0−1 T as well as the magnetic ordering temperatures is plotted in Figure 1b for $ErFe_2Si_2$ compared with other reported MCE compounds. Clearly, among all of the reported MCE materials at a 0−1 T field change, only $ErFe_2Si_2$, TmCuAl, TmCoSi, and HoNiSi have magnetic ordering temperatures lower than the liquid helium temperature (4.2 K). For magnetocaloric materials, the magnetic ordering temperature usually corresponds to the peak on $(-\Delta S_M)_{max}$ curves and can be evaluated as the working temperature for magnetic cooling. Therefore, $ErFe_2Si_2$, together with the previously reported TmCuAl, TmCoSi, and HoNiSi, can be classified into liquid-helium-temperature magnetic refrigerant materials. As Figure 1b shows, the $(-\Delta S_M)_{max}$ of $ErFe_2Si_2$ under a field change of 0−1 T is competitive with other present liquid-helium-temperature magnetocaloric materials, which makes it a potential candidate to be used for the liquefaction of gaseous helium.

In order to analyze the correlation between the magnetic ground state and the MCE, the magnetic entropy change under field changes lower than 0−1 T was also calculated and is shown in a contour plot in Figure 5b. It can be seen that the positive magnetic entropy change is obtained under field changes lower than 0−0.6 T, which is known as the inverse MCE.[40−42] The maximum value of the positive magnetic entropy change is 4.7 J/kg K at 2.25 K under a field change of 0−0.3 T. As the field change increases, the maximum value of the positive magnetic entropy change diminishes monotonically and becomes zero, and the temperature range of the inverse MCE also shrinks. With further increasing of the field change, the magnetic entropy change becomes negative and the inverse MCE is converted into the normal MCE. Since the peak value of the positive magnetic entropy change is located at low temperatures, the inverse MCE should be related to the AFM ground state. In fact, the inverse MCE is an inevitable result of AFM materials under a magnetic field, which has been reported in many AFM materials such as $ErRu_2Si_2$[43] and Dy_3Co.[44] AFM ordering is a state with a high degree of spin ordering, which would be disturbed by an external magnetic field. As the degree of ordering is lower and the disorder/randomness increases, the positive magnetic entropy change is observed. When the magnetic field exceeds a critical value, which just corresponds to the critical field of the metamagnetic transition, the magnetic ordering is destroyed completely. As the magnetic field is further increased, a new type of interaction begins to establish; thus, the normal MCE is observed.

The magnetic entropy change can also be calculated based on the specific heat data according to the modified method.[45,46] First, the total entropy is calculated based on the specific heat measured at 0 and 1 T, respectively, by integrating C_p/T:

https://doi.org/10.1021/acs.chemmater.3c03079
Chem. Mater. 2024, 36, 1707−1718

$$S(H = 0T, T) = \frac{1}{2}C_p(H = 0T, T_0) + \int_{T_0}^{T} \frac{C_p(H = 0T, T)}{T} dT \quad (4)$$

$$S(H = 1T, T) = \frac{1}{2}C_p(H = 1T, T_0) + \int_{T_0}^{T} \frac{C_p(H = 1T, T)}{T} dT \quad (5)$$

where T_0 is the lowest temperature to measure the specific heat. Then, the magnetic entropy change can be obtained by integrating the difference of C_p/T:

$$\Delta S_M(T) = S(H = 1T, T) - S(H = 0T, T) = \frac{1}{2}\Delta C_p(T_0) + \int_{T_0}^{T} \frac{\Delta C_p(T)}{T} dT \quad (6)$$

The magnetic entropy change curve calculated from the specific heat data is shown in Figure 5c and the temperature dependence of $-\Delta C_p/T$ is presented in the inset of Figure 5c. Comparing Figure 5a,c, it is noticeable that the $-\Delta S_M$ values calculated from the magnetic data and from the specific heat data are not exactly the same, although the shapes of these $-\Delta S_M$ curves are consistent with each other. The peak of the $-\Delta S_M$ curve, whether calculated from the magnetic data or calculated from the specific heat data, is at 3.2 K, which is also the zero point of ΔC_p, as shown in the inset of Figure 5c. In fact, this temperature is also the cross point of the C_p curves measured at 0 and 1 T, as shown in Figure 3b. Therefore, the peak of the $-\Delta S_M$ curve is not located exactly at the temperature of the C_p peak but slightly higher than it.

The adiabatic temperature change (ΔT_{ad}) is another parameter to quantitatively evaluate the MCE and it can be obtained by taking subtraction of the temperature from the $S-T$ curve.[46] Since the specific heat at high fields was not measured, a modified method to calculate the ΔT_{ad} based on both magnetic data and heat capacity data was employed.[47] First, the total entropy at zero field is calculated from the zero-field specific heat data according to eq 4. Then, the total entropy at high field is calculated by adding the ΔS_M to the zero-field total entropy:

$$S(H, T) = S(H = 0T, T) + \Delta S_M \quad (7)$$

where the ΔS_M value is obtained from the magnetic data. Finally, the ΔT_{ad} can be obtained according to the following formula:

$$\Delta T_{ad} = T(S, H) - T(S, H = 0T) \quad (8)$$

where $T(S, H)$ is the inverse function of $S(H, T)$. The temperature-dependent ΔT_{ad} curves under different field changes are plotted in Figure 5d. The maximum points of the ΔT_{ad} are determined to be 5.7, 10.5, 13.8, 16.3, 18.1, 19.7, and 21.0 K for a field change of 0−1, 0−2, 0−3, 0−4, 0−5, 0−6, and 0−7 T, respectively. The variation tendency of the ΔT_{ad} is similar to that of the $-\Delta S_M$ and there is also a long tail on the high-temperature side of the ΔT_{ad} curve, indicating that short-range interaction has influence on the adiabatic temperature change as well. To compare the maximum value of the ΔT_{ad} ($(\Delta T_{ad})_{max}$) with other low-temperature magnetocaloric materials, the $(\Delta T_{ad})_{max}$ under field changes of 0−1 and 0−5 T are also listed in Table 2. It is found that the $(\Delta T_{ad})_{max}$ of $ErFe_2Si_2$ is much larger than those of the typical low-temperature magnetocaloric materials under a field change of 0−5 T. As for the field change of 0−1 T, the advantage of $ErFe_2Si_2$ is still comparable to TmCoSi and much larger than $ErMn_2Si_2$, $TmMn_2Si_2$, HoB_2, TmGa, and ErNiBC. Therefore, the low-field ΔT_{ad} of $ErFe_2Si_2$ is also competitive among the low-temperature MCE materials. In particular, although the $(-\Delta S_M)_{max}$ of $ErFe_2Si_2$ is lower than those of $ErMn_2Si_2$, HoB_2, and TmGa, the $(\Delta T_{ad})_{max}$ of $ErFe_2Si_2$ is much superior. Therefore, the overall MCE performance indicates that the $ErFe_2Si_2$ compound is a potentially suitable magnetocaloric material for low-temperature magnetic cooling.

Theoretical calculations were also employed to verify which type of magnetic structure is most stable for the $ErFe_2Si_2$ compound. To simplify the calculation work, the systematic energy of each of the aforementioned 4 specific magnetic models was calculated separately. 1×1×2 unit cells were constructed during the calculations. The magnetic structure was initialized as cases A1, A2, B1, and B2, respectively. Neither the direction nor the value of the magnetic moments was constrained. After structural optimization, all four cases converged. The detailed magnetic moments of each Er atom in the unit cell for all four cases are listed in Table 3. It can be seen that all four types of magnetic structures after optimization are close to the initial states, indicating that they can exist stably. Furthermore, the calculated systematic energy is −151.427, −154.168, −154.708, and −154.679 eV for cases A1, A2, B1, and B2, respectively, as presented in Table 3. It is found that case B1 has the lowest systematic energy among the four cases, indicating that case B1 is possibly the most likely form of the magnetic structure in $ErFe_2Si_2$.

Table 3. Four Types of Magnetic Structures after Structural Optimization and the Corresponding Systematic Energy Based on the First-Principles Calculations. Er1, Er2, Er3, and Er4 Correspond to the Er Atoms with *z*-Coordinates of 0, 0.5, 1.0, and 1.5 in the Superlattice Cell, Respectively

	case A1		case A2		case B1		case B2	
	M_x	M_y	M_x	M_y	M_x	M_y	M_x	M_y
Er1/μ_B	7.8	0.0	8.8	0.0	7.8	0.0	5.3	5.3
Er2/μ_B	0.0	0.0	−8.8	0.0	0.0	7.8	−5.3	5.3
Er3/μ_B	−7.8	0.0	−8.8	0.0	−7.8	0.0	−5.3	−5.3
Er4/μ_B	0.0	0.0	8.8	0.0	0.0	−7.8	5.3	−5.3
E/eV	−151.427		−154.168		−154.708		−154.679	

A giant low-field MCE is an important and applicable feature for magnetocaloric materials; therefore, it is crucial to understand the underlying physical mechanism of the giant low-field MCE observed in the present $ErFe_2Si_2$ compound. We believe that $ErFe_2Si_2$ exhibits a giant MCE under a low-field change, such as 0−1 T, for the following reasons. First, the critical magnetic field for the metamagnetic transition is very low. It is known that the magnetic ground state of $ErFe_2Si_2$ is AFM. As shown in Figure 5b, it experiences the inverse and normal MCE sequentially with increasing magnetic field as the increase of the magnetic field results in the positive ΔS_M below the H_{cr} and the negative ΔS_M at high fields. The H_{cr} has been determined to be 0.3 T at 2 K for $ErFe_2Si_2$, indicating that AFM ordering begins to be destroyed and FM ordering starts to be constructed as the external magnetic field exceeds 0.3 T since the critical magnetic field is the ending point of AFM ordering and the beginning point of FM

https://doi.org/10.1021/acs.chemmater.3c03079
Chem. Mater. 2024, 36, 1707−1718

ordering. The low H_{cr} is attributed to the possible special magnetic structures together with the short-range interaction in the $ErFe_2Si_2$ compound. When the magnetic field reaches 1 T, the observed inverse MCE completely transforms to a normal MCE. Second, $ErFe_2Si_2$ is easy to be magnetized to a quasi-saturation state. It has been discussed that the magnetization with a temperature of 2 K at 1 T reaches 104.6 Am^2/kg, which is as high as 81.2% of that at 7 T (128.8 Am^2/kg), indicating that magnetic ordering can be easily driven by a low magnetic field. The field of 1 T can be described as a quasi-saturation magnetic field for simplification. Hence, under a field of 1 T, the $ErFe_2Si_2$ compound can step from a state with a high degree of disorder into a state with a high degree of magnetic ordering. Such a variation in the degree of magnetic ordering contributes to the magnetic entropy change, which is used to evaluate the MCE. Therefore, both the low critical magnetic field for metamagnetic transition and the low quasi-saturation magnetic field lead to the excellent low-field MCE performance of the $ErFe_2Si_2$ compound.

Good heat reversibility and magnetic reversibility have been observed in $ErFe_2Si_2$, as shown in Figures 3a and S1. This may be ascribed to the possible presence of the second-order magnetic transition, which usually signals ignorable heat and magnetic hysteresis in these materials. Therefore, the characteristics of the magnetic transition were analyzed using several theoretical models. First, Arrott plots were employed to reveal the feature of the second-order magnetic transition, as shown in Figure S10. According to Banerjee's criterion,[48] the magnetic transition is second order if the slope of Arrott plots around the magnetic ordering temperature is positive, otherwise it is first order. It is clear that these curves show a positive slope; thus, they have the feature of the second-order magnetic transition. Although negative slopes are observed at 2 and 2.5 K, they are caused by the field-induced metamagnetic transition and will not affect the overall analyses on the type of magnetic transition. Second, a rescaled universal curve is plotted in Figure S11 and it was also employed to confirm the characteristic of the second-order phase transition. It is proposed that the rescaled magnetic entropy change curves under different field changes will overlap with each other if the magnetic phase transition is second order.[49] The normalized and rescaled experimental $-\Delta S_M$ curves are obtained using the method described in other works.[50] The above curves under different field changes collapse into a universal one, indicating the presence of the second-order phase transition. Third, the mean field theory was also used to analyze the type of magnetic phase transition. The $(\mu_0 H)^{2/3}$ dependence of the $-\Delta S_M$ around T_N, as shown in Figure S12, nearly obeys a linear relationship, which indicates a typical second-order transition system according to the mean field theory. Therefore, these three types of analysis methods all confirm the characteristic second-order phase transition in $ErFe_2Si_2$.

CONCLUSIONS

The polycrystal $ErFe_2Si_2$ compound was synthesized by the arc-melting method. The purity and the homogeneity of the sample were confirmed based on XRD and SEM experiments. The magnetic ground state of $ErFe_2Si_2$ is determined as AFM by a thermal magnetization curve with a Néel temperature of 3.0 K. The isothermal magnetization curve further confirms the AFM ordering of $ErFe_2Si_2$ and also reveals the signal of short-range interaction. NPD experiments at different temperatures indicate that the magnetic structure of $ErFe_2Si_2$ is not unique and different types of magnetic ordering such as TSDW and spiral models can indistinguishably fit the NPD patterns. Four specific cases of magnetic structures are further discussed based on the first-principles calculations. The calculations show that the models other than case A1 cannot be distinguished as well. In addition, $ErFe_2Si_2$ exhibits a giant low-field magnetocaloric effect. The $(-\Delta S_M)_{max}$ and $(\Delta T_{ad})_{max}$ under a field change of 0−1 T are determined as 11.5 J/kg K and 5.7 K, respectively, which are comparable to those of the best low-temperature magnetocaloric materials. The giant low-field MCE of $ErFe_2Si_2$ should be related to its low critical field of metamagnetic transition and the low magnetic field required for saturation. $ErFe_2Si_2$ also shows a second-order magnetic transition, which is confirmed by three independent criteria. The collective excellent performance of $ErFe_2Si_2$ indicates that it is a promising magnetocaloric material for applications at liquid helium temperatures.

EXPERIMENTAL SECTION

Sample Preparation. The polycrystalline $ErFe_2Si_2$ compound was synthesized by arc-melting Er, Fe, and Si elementary substances with a purity higher than 99.9 wt %. Due to the volatilization, 2% of Er was overadded into the stoichiometric amounts of the mixture before melting. To ensure homogeneity, the ingot was melted 4 times, annealed at 1073 K for 7 days, and then quenched with liquid nitrogen. To verify the purity of the sample and examine the crystal structure, room-temperature X-ray diffraction (XRD) with Cu−Kα radiation (wavelength λ = 1.5406 Å) and energy-dispersive spectroscopy (EDS) measurements on a field emission scanning electron microscope (SEM) were carried out.

Neutron Powder Diffraction (NPD) Measurements. NPD was performed at different temperatures ranging from 2 to 10 K on the general purpose powder diffractometer (GPPD) at the China Spallation Neutron Source (CSNS) in Dongguan, China. Samples were loaded in 9.1 mm vanadium cans, and experimental data were collected at different temperatures in the time-of-fight (TOF) mode with wavelength bands of 0.1−4.9 Å. The diffraction patterns were collected by detector arrays marked as bank A and bank B with diffraction angles 2θ of 90 and 30°, respectively. The programs GSAS and Fullprof were used for the Rietveld refinement of crystal and magnetic structures.

Magnetic Property Measurements. Magnetization measurements were performed by using a vibrating sample magnetometer with quantum design (SQUID-VSM) and the specific heat data was collected by a physical property measurement system (PPMS). The sweep rate of the thermal magnetization measurement was 1 K/min. As for the specific heat measurement, the variation of temperature was not uniform because each data was obtained with different time durations from 3 to 20 min. The isothermal magnetization measurements were performed by a stable mode at each point with an applied magnetic field up to 7 T.

ASSOCIATED CONTENT

Data Availability Statement

Experimental data files are available upon reasonable request from the corresponding author.

Supporting Information

The Supporting Information is available free of charge at https://pubs.acs.org/doi/10.1021/acs.chemmater.3c03079.

Materials and methods, isothermal magnetization curves, NPD patterns and Rietveld refinement fitting curves at 2 K based on four different models, NPD patterns and Rietveld refinement fitting curves at different temperatures, Arrott plot, rescaled universal curves, the

https://doi.org/10.1021/acs.chemmater.3c03079
Chem. Mater. 2024, 36, 1707−1718

$(\mu_0 H)^{2/3}$ dependence of the $-\Delta SM$, and the table of refined parameters for four models (PDF)

AUTHOR INFORMATION

Corresponding Authors

X. Q. Zheng − *School of Materials Science and Engineering, Key Laboratory of Advanced Materials and Devices for Post-Moore Chips Ministry of Education, University of Science and Technology Beijing, Beijing 100083, China;* orcid.org/0000-0002-1894-4910; Email: zhengxq@ustb.edu.cn

S. G. Wang − *School of Materials Science and Engineering, Key Laboratory of Advanced Materials and Devices for Post-Moore Chips Ministry of Education, University of Science and Technology Beijing, Beijing 100083, China; Anhui Key Laboratory of Magnetic Functional Materials and Devices, School of Materials Science and Engineering, Anhui University, Hefei 230601, China*; Email: sgwang@ustb.edu.cn

B. G. Shen − *Beijing National Laboratory for Condensed Matter Physics, Institute of Physics, Chinese Academy of Sciences & University of Chinese Academy of Sciences, Beijing 100190, China; Anhui Key Laboratory of Magnetic Functional Materials and Devices, School of Materials Science and Engineering, Anhui University, Hefei 230601, China; Ningbo Institute of Materials Technology and Engineering, Chinese Academy of Sciences, Ningbo 315201, China;* orcid.org/0000-0003-4819-1806; Email: shenbg@iphy.ac.cn

Authors

D. S. Wang − *School of Materials Science and Engineering, Key Laboratory of Advanced Materials and Devices for Post-Moore Chips Ministry of Education, University of Science and Technology Beijing, Beijing 100083, China; Beijing National Laboratory for Condensed Matter Physics, Institute of Physics, Chinese Academy of Sciences & University of Chinese Academy of Sciences, Beijing 100190, China*

J. W. Xu − *Anhui Key Laboratory of Magnetic Functional Materials and Devices, School of Materials Science and Engineering, Anhui University, Hefei 230601, China*

L. H. He − *Beijing National Laboratory for Condensed Matter Physics, Institute of Physics, Chinese Academy of Sciences & University of Chinese Academy of Sciences, Beijing 100190, China; Spallation Neutron Source Science Center, Dongguan 523803, China; Songshan Lake Materials Laboratory, Dongguan 523808, China*

Y. W. Gao − *School of Materials Science and Engineering, Key Laboratory of Advanced Materials and Devices for Post-Moore Chips Ministry of Education, University of Science and Technology Beijing, Beijing 100083, China*

H. Huang − *School of Materials Science and Engineering, Key Laboratory of Advanced Materials and Devices for Post-Moore Chips Ministry of Education, University of Science and Technology Beijing, Beijing 100083, China;* orcid.org/0000-0003-1335-3174

H. Wu − *NIST Center for Neutron Research, National Institute of Standards and Technology, Gaithersburg 20899, United States*

X. Y. Cao − *School of Materials Science and Engineering, Key Laboratory of Advanced Materials and Devices for Post-Moore Chips Ministry of Education, University of Science and Technology Beijing, Beijing 100083, China*

D. Liu − *Department of Physics, Beijing Technology and Business University, Beijing 100048, China*

J. X. Shen − *School of Materials Science and Engineering, Key Laboratory of Advanced Materials and Devices for Post-Moore Chips Ministry of Education, University of Science and Technology Beijing, Beijing 100083, China*

G. Y. Wang − *School of Materials Science and Engineering, Key Laboratory of Advanced Materials and Devices for Post-Moore Chips Ministry of Education, University of Science and Technology Beijing, Beijing 100083, China; Ningbo Institute of Materials Technology and Engineering, Chinese Academy of Sciences, Ningbo 315201, China*

J. Y. Zhang − *School of Materials Science and Engineering, Key Laboratory of Advanced Materials and Devices for Post-Moore Chips Ministry of Education, University of Science and Technology Beijing, Beijing 100083, China;* orcid.org/0000-0003-0012-6191

Y. F. Wu − *School of Materials Science and Engineering, Key Laboratory of Advanced Materials and Devices for Post-Moore Chips Ministry of Education, University of Science and Technology Beijing, Beijing 100083, China;* orcid.org/0000-0002-2081-8091

F. X. Hu − *Beijing National Laboratory for Condensed Matter Physics, Institute of Physics, Chinese Academy of Sciences & University of Chinese Academy of Sciences, Beijing 100190, China;* orcid.org/0000-0003-0383-0213

Complete contact information is available at: https://pubs.acs.org/10.1021/acs.chemmater.3c03079

Notes

The authors declare no competing financial interest.

ACKNOWLEDGMENTS

This work was partially supported by the National Key Research and Development Program of China (MOST) (Nos. 2023YFA1610400 and 2021YFB3501202), the Science Center of the National Science Foundation of China (No. 52088101), and the National Natural Science Foundation of China (Nos. 52171170, 51871019, 52130103, 51971026, U23A20550, 92263202). We thank Qingzhen Huang for the discussions on the analysis of magnetic structure.

REFERENCES

(1) Yang, S. X.; Zheng, X. Q.; Xi, L.; Wang, D. S.; Liu, C. F.; Xu, J. W.; Wang, L. C.; Xu, Z. Y.; Zhang, J. Y.; Wu, Y. F.; Shen, J. X.; Huang, H.; Wang, S. G.; Shen, B. G. Effect of In or Ge substitution on magnetic ordering in TmGa(In/Ge) compounds. *J. Alloys Compd.* **2022**, *897*, No. 163236.

(2) Kumar, S.; Patrick, C. E.; Edwards, R. S.; Balakrishnan, G.; Lees, M. R.; Staunton, J. B. Torque magnetometry study of the spin reorientation transition and temperature-dependent magnetocrystalline anisotropy in $NdCo_5$. *J. Phys.: Condens. Matter* **2020**, *32*, No. 255802.

(3) Nakamura, S.; Kabeya, N.; Kobayashi, M.; Araki, K.; Katoh, K.; Ochiai, A. Magnetic phases of the frustrated ferromagnetic spin-trimer system $Gd_3Ru_4Al_{12}$ with a distorted kagome lattice structure. *Phys. Rev. B* **2023**, *107*, No. 014422.

(4) Shiina, R. *International Conference on Strongly Correlated Electron Systems (SCES)*; Cambridge: ENGLAND, 2012; Vol. *391*.

(5) Gao, F.; Sheng, J. M.; Ren, W. J.; Zhang, Q.; Luo, X. H.; Qi, J.; Cong, M. R.; Li, B.; Wu, L. S.; Zhang, Z. D. Incommensurate spin density wave and magnetocaloric effect in the metallic triangular lattice $HoAl_2Ge_2$. *Phys. Rev. B* **2022**, *106*, No. 134426.

(6) Trovarelli, O.; Sereni, J. G.; Pureur, P.; Shaf, J. Evidence of spin-density-wave to spin-glass transformation in YNd Alloys. *Phys. Rev. B* **1995**, *52*, 15387.
(7) Waite, R.; Orlandi, F.; Sokolov, D. A.; Ribeiro, R. A.; Canfield, P. C.; Manuel, P.; Khalyavin, D. D.; Hicks, C. W.; Hayden, S. M. Spin-density-wave order controlled by uniaxial stress in $CeAuSb_2$. *Phys. Rev. B* **2022**, *106*, No. 224415.
(8) Leciejewicz, J.; Stüsser, N.; Kolenda, M.; Szytuła, A.; Zygmunt, A. Magnetic ordering in HoCoSi and TbCoGe. *J. Alloys Compd.* **1996**, *240*, 164.
(9) Schobinger-Papamantellos, P.; Rodríguez-Carvajal, J.; Buschow, K. H. J. Cycloid spirals and cycloid cone transition in the $HoMn_{6-x}Cr_xGe_6$ (T, x) magnetic phase diagramm by neutron diffraction. *J. Magn. Magn. Mater.* **2016**, *408*, 233−243.
(10) Semitelou, J. P.; Yakinthos, J. K. The conical magnetic structure of Dy_5Si_3. *J. Magn. Magn. Mater.* **2003**, *265*, 152.
(11) Pecharsky, V. K.; Gschneidner, K. A.; Pecharsky, A. O.; Tishin, A. M. Thermodynamics of the magnetocaloric effect. *Phys. Rev. B* **2001**, *64*, No. 144406.
(12) Gschneidner, K. A., Jr.; Pecharsky, V. K. Magnetocaloric materials. *Annu. Rev. Mater. Sci.* **2000**, *30*, 387.
(13) Felner, I.; Mayer, I.; Grill, A.; Schieber, M. Magnetic ordering in rare earth Iron Silicides and Germanides of the RFe_2X_2 type. *Solid State Commun.* **1975**, *16*, 1005.
(14) Umarji, A. M.; Noakes, D. R.; Viccaro, P. J.; Shenoy, G. K.; Aldred, A. T.; Niarchos, D. Magnetic properties of $REFe_2Si_2$ compounds. *J. Magn. Magn. Mater.* **1983**, *36*, 61.
(15) Pinto, H.; Melamud, M.; Kuznietz, M.; Shaked, H. Magnetic structures in the ternary RM_2X_2 compounds (R = Gd to Tm; M = Fe, Co, Ni, or Cu; X = Si or Ge). *Phys. Rev. B* **1985**, *31*, 508.
(16) Szytula, A.; Leciejewicz, J.; Gschneidner, K. A.; Eyring, L., Eds. 1989.
(17) Noakes, D. R.; Umarji, A. M.; Shenoy, G. K. Mössbauer studies of $REFe_2Si_2$ (RE = Gd-Lu) compounds. *J. Magn. Magn. Mater.* **1983**, *39*, 309.
(18) Leciejewicz, J.; Siek, S.; Szytula, A. Neutron diffraction study of magnetic ordering in $ErMn_2Si_2$, $ErMn_2Ge_2$ and $ErFe_2Si_2$. *J. Magn. Magn. Mater.* **1984**, *40*, 265.
(19) Chen, J.; Shen, B. G.; Dong, Q. Y.; Hu, F. X.; Sun, J. R. Large reversible magnetocaloric effect caused by two successive magnetic transitions in ErGa compound. *Appl. Phys. Lett.* **2009**, *95*, No. 132504.
(20) Liu, Y.; Zheng, X.; Liang, F.; Hu, F.; Huang, Q.; Li, Z.; Liu, J. Large barocaloric effect in intermetallic $La_{1.2}Ce_{0.8}Fe_{11}Si_2H_{1.86}$ materials driven by low pressure. *NPG Asia Mater.* **2022**, *14*, No. 30.
(21) Mihalik, M.; Svoboda, P.; Mihalik, M.; Vejpravová, J.; Sechovský, V. Magnetic and transport properties of $GdFe_2Si_2$ single-crystal. *J. Magn. Magn. Mater.* **2005**, *290*−*291*, 606.
(22) Mihalik, M.; Vejpravová, J.; Rusz, J.; Diviš, M.; Svoboda, P.; Sechovský, V.; Mihalik, M. Anisotropic magnetic properties and specific-heat study of a $TbFe_2Si_2$ single crystal. *Phys. Rev. B* **2004**, *70*, No. 134405.
(23) Zheng, X. Q.; Xu, J. W.; Zhang, H.; Zhang, J. Y.; Wang, S. G.; Zhang, Y.; Xu, Z. Y.; Wang, L. C.; Shen, B. G. Magnetic properties and magnetocaloric effect of $HoCo_3B_2$ compound. *AIP Adv.* **2018**, *8*, No. 056432.
(24) Chen, J.; Shen, B. G.; Dong, Q. Y.; Hu, F. X.; Sun, J. R. Giant reversible magnetocaloric effect in metamagnetic HoCuSi compound. *Appl. Phys. Lett.* **2010**, *96*, No. 152501.
(25) Li, L.; Nishimura, K.; Hutchison, W. D.; Qian, Z.; Huo, D.; NamiKi, T. Giant reversible magnetocaloric effect in $ErMn_2Si_2$ compound with a second order magnetic phase transition. *Appl. Phys. Lett.* **2012**, *100*, No. 152403.
(26) Li, L.; Saensunon, B.; Hutchison, W. D.; Huo, D.; Nishimura, K. Magnetic properties and large reversible magnetocaloric effect in $TmMn_2Si_2$. *J. Alloys Compd.* **2014**, *582*, 670.
(27) Li, L.; Yuan, Y.; Zhang, Y.; Namiki, T.; Nishimura, K.; Pöttgen, R.; Zhou, S. Giant low field magnetocaloric effect and field-induced metamagnetic transition in TmZn. *Appl. Phys. Lett.* **2015**, *107*, No. 132401.
(28) Mo, Z. J.; Shen, J.; Yan, L. Q.; Wu, J. F.; Wang, L. C.; Lin, J.; Tang, C. C.; Shen, B. G. Low-field induced giant magnetocaloric effect in TmCuAl compound. *Appl. Phys. Lett.* **2013**, *102*, No. 192407.
(29) Xu, J. W.; Zheng, X. Q.; Yang, S. X.; Xi, L.; Zhang, J. Y.; Wu, Y. F.; Wang, S. G.; Liu, J.; Wang, L. C.; Xu, Z. Y.; Shen, B. G. Giant low field magnetocaloric effect in TmCoSi and TmCuSi compounds. *J. Alloys Compd.* **2020**, *843*, No. 155930.
(30) de Castro, P. B.; Terashima, K.; Yamamoto, T. D.; Hou, Z.; Iwasaki, S.; Matsumoto, R.; Adachi, S.; Saito, Y.; Song, P.; Takeya, H.; Takano, Y. Machine-learning-guided discovery of the gigantic magnetocaloric effect in HoB_2 near the hydrogen liquefaction temperature. *NPG Asia Mater.* **2020**, *12*, 35.
(31) Mo, Z. J.; Shen, J.; Yan, L. Q.; Tang, C. C.; Lin, J.; Wu, J. F.; Sun, J. R.; Wang, L. C.; Zheng, X. Q.; Shen, B. G. Low field induced giant magnetocaloric effect in TmGa compound. *Appl. Phys. Lett.* **2013**, *103*, No. 052409.
(32) Li, D. X.; Yamamura, T.; Nimori, S.; Homma, Y.; Honda, F.; Haga, Y.; Aoki, D. Large reversible magnetocaloric effect in ferromagnetic semiconductor EuS. *Solid State Commun.* **2014**, *193*, 6.
(33) Wang, L. C.; Dong, Q. Y.; Mo, Z. J.; Xu, Z. Y.; Hu, F. X.; Sun, J. R.; Shen, B. G. Low-temperature reversible giant magnetocaloric effect in the HoCuAl compound. *J. Appl. Phys.* **2013**, *114*, No. 163915.
(34) Meng, L.; Xu, C.; Yuan, Y.; Qi, Y.; Zhou, S.; Li, L. Magnetic properties and giant reversible magnetocaloric effect in $GdCoC_2$. *RSC Adv.* **2016**, *6*, 74765.
(35) Zhang, H.; Wu, Y.; Long, Y.; Wang, H.; Zhong, K.; Hu, F.; Sun, J.; Shen, B. Large reversible magnetocaloric effect in antiferromagnetic HoNiSi compound. *J. Appl. Phys.* **2014**, *116*, No. 213902.
(36) Zhang, Y.; Wilde, G. Magnetic properties and magnetocaloric effect in quaternary boroncarbides compound ErNiBC. *Phys. B* **2015**, *472*, 56.
(37) Lionte, S.; Risser, M.; Muller, C. A 15 kW magnetocaloric proof-of-concept unit: Initial development and first experimental results. *Int. J. Refrig.* **2021**, *122*, 256.
(38) Maiorino, A.; Mauro, A.; Del Duca, M. G.; Mota-Babiloni, A.; Aprea, C. Looking for energy losses of a rotary permanent magnet magnetic refrigerator to optimize its performances. *Energies* **2019**, *12*, 4388.
(39) Shen, J.; Gao, X. Q.; Li, K.; Dai, W.; Li, Z. X.; Mo, Z. J.; Zheng, X. Q.; Gong, M. Q. Experimental research on a 4 K hybrid refrigerator combining GM gas refrigeration effect with magnetic refrigeration effect. *Cryogenics* **2019**, *99*, 99.
(40) Krenke, T.; Duman, E.; Acet, M.; Wassermann, E. F.; Moya, X.; Mañosa, L.; Planes, A. Inverse magnetocaloric effect in ferromagnetic Ni−Mn−Sn alloys. *Nat. Mater.* **2005**, *4*, 450.
(41) Biniskos, N.; Schmalzl, K.; Raymond, S.; Petit, S.; Steffens, P.; Persson, J.; Bruckel, T. Spin Fluctuations Drive the Inverse Magnetocaloric Effect in Mn_5Si_3. *Phys. Rev. Lett.* **2018**, *120*, No. 257205.
(42) Biswas, A.; Chandra, S.; Samanta, T.; Ghosh, B.; Datta, S.; Phan, M. H.; Raychaudhuri, A. K.; Das, I.; Srikanth, H. Universality in the entropy change for the inverse magnetocaloric effect. *Phys. Rev. B* **2013**, *87*, No. 134420.
(43) Samanta, T.; Das, I.; Banerjee, S. Giant magnetocaloric effect in antiferromagnetic $ErRu_2Si_2$ compound. *Appl. Phys. Lett.* **2007**, *91*, No. 152506.
(44) Shen, J.; Zhao, J. L.; Hu, F. X.; Rao, G. H.; Liu, G. Y.; Wu, J. F.; Li, Y. X.; Sun, J. R.; Shen, B. G. Magnetocaloric effect in antiferromagnetic Dy_3Co compound. *Appl. Phys. A: Mater. Sci. Process.* **2010**, *99*, 853.
(45) Moreno-Ramírez, L. M.; Franco, V.; Conde, A.; Neves Bez, H.; Mudryk, Y.; Pecharsky, V. K. Influence of the starting temperature of calorimetric measurements on the accuracy of determined magnetocaloric effect. *J. Magn. Magn. Mater.* **2018**, *457*, 64.
(46) Pecharsky, V. K.; Gschneidner, K. A. Magnetocaloric effect from indirect measurements Magnetization and heat capacity. *J. Appl. Phys.* **1999**, *86*, 565.

https://doi.org/10.1021/acs.chemmater.3c03079
Chem. Mater. 2024, 36, 1707−1718

(47) Zheng, X. Q.; Chen, J.; Xu, Z. Y.; Mo, Z. J.; Hu, F. X.; Sun, J. R.; Shen, B. G. Nearly constant magnetic entropy change and adiabatic temperature change in PrGa compound. *J. Appl. Phys.* **2014**, *115*, No. 17A938.
(48) Banerjee, S. K. On a generalised approach to first and second order magnetic transitions. *Phys. Lett.* **1964**, *12*, 16.
(49) Franco, V.; Conde, A.; Romero-Enrique, J. M.; Blázquez, J. S. A universal curve for the magnetocaloric effect: an analysis based on scaling relations. *J. Phys.: Condens. Matter* **2008**, *20*, No. 285207.
(50) Yang, S. X.; Zheng, X. Q.; Wang, D. S.; Xu, J. P.; Yin, W.; Xi, L.; Liu, C. F.; Liu, J.; Xu, J. W.; Zhang, H.; Xu, Z. Y.; Wang, L. C.; Yao, Y. H.; Zhang, M. S.; Zhang, Y. C.; Shen, J. X.; Wang, S. G.; Shen, B. G. Giant low-field magnetocaloric effect in ferromagnetically ordered $Er_{1-x}TmxAl_2$ $(0 \leq x \leq 1)$ compounds. *J. Mater. Sci. Technol.* **2023**, *146*, 168−176.

https://doi.org/10.1021/acs.chemmater.3c03079
Chem. Mater. 2024, 36, 1707−1718